

Design and Evaluation of a Portable Intra-Operative Unified-Planning-and-Guidance Framework Applied to Distal Radius Fracture Surgery

Jessica Magaraggia · Wei Wei · Markus Weiten · Gerhard Kleinszig ·
Sven Vetter · Jochen Franke · Adrian John · Adrian Egli · Karl Barth ·
Elli Angelopoulou · Joachim Hornegger

Received: date / Accepted: date

Abstract *Purpose* During a standard fracture reduction and fixation procedure of the distal radius, only fluoroscopic images are available for planning of the screw placement and monitoring of the drill bit trajectory. Our prototype intra-operative framework integrates planning and drill guidance for a simplified and improved planning transfer.

Methods Guidance information is extracted using a video-camera mounted onto a surgical drill. Real-time feedback of the drill-bit position is provided using an augmented view of the planning X-rays. We evaluate the accuracy of the placed screws on plastic bones, and on healthy and fractured forearm specimens. We also investigate the difference in accuracy between guided

screw-placement versus freehand. Moreover, the accuracy of the real-time position feedback of the drill bit is evaluated.

Results A total of 166 screws were placed. On 37 plastic bones, our obtained accuracy was 1.01 ± 0.56 mm, $3.74 \pm 4.39^\circ$ and $1.70 \pm 1.35^\circ$ in tip position and orientation (azimuth and elevation) respectively. On the 3 healthy forearm specimens, our obtained accuracy was 1.63 ± 0.91 mm, $5.85 \pm 4.93^\circ$ and $3.48 \pm 3.07^\circ$. On the 2 fractured specimens, we attained: 1.39 ± 0.47 mm, $2.93 \pm 1.83^\circ$ and $2.14 \pm 1.84^\circ$. When screw plans were applied freehand (without our guidance system) the achieved accuracy was 1.73 ± 0.82 mm, $6.01 \pm 4.94^\circ$, $3.52 \pm 2.48^\circ$, while when they were transferred under guidance we obtained: 0.89 ± 0.37 mm, $2.85 \pm 2.57^\circ$, $1.49 \pm 1.17^\circ$.

Conclusions Our results show that our framework is expected to increase the accuracy in screw positioning and to improve robustness w.r.t. freehand placement.

Keywords Intra-operative Planning · Intra-operative Guidance · Orthopedic Surgery · Trauma Surgery

J. Magaraggia · E. Angelopoulou · J. Hornegger
Pattern Recognition Lab, Friedrich-Alexander University
Erlangen-Nürnberg, Martensstr. 3, 91058 Erlangen, Germany,
E-mail: jessica.magaraggia@cs.fau.de

J. Magaraggia
Graduiertenkolleg 1773 “Heterogene Bildsysteme”, Cauerstr.
11, 91058 Erlangen, Germany,

W. Wei · M. Weiten · G. Kleinszig · K. Barth
Siemens Healthcare GmbH, Roethelheimpark Alle 2, 91052
Erlangen, Germany,

S. Vetter · J. Franke
Klinik für Unfallchirurgie und Orthopädie, BG Klinik
Ludwigshafen, Ludwig-Guttman-Straße 13, 67071 Ludwigshafen,
Germany

The presented method is investigational use and is limited by law to investigational use. It is not commercially available and its future availability cannot be ensured. The source code for the presented methods is not publicly or commercially available and its future availability cannot be ensured.

1 Introduction

Fractures to the distal radius account for up to 15% of all the extremity fractures. According to McKay et al. [22], the number of complications can range from 6% to 80%. The treatment of distal radius fractures commonly involves an open reduction and internal fixation (ORIF) surgery [29]. The steps of a standard ORIF are summarized in Fig. 1. First, the fracture is exposed and reduced, i.e. the bone fragments are re-aligned. During internal fixation, a fixation plate is fixed onto the bone shaft using one or two cortical screws at the proximal side of the plate. The correct plate positioning is

usually confirmed using X-ray images before the cortical screws are finally tightened. Afterwards, the fixation screws are inserted. The direction and length of each screw are determined using X-ray images acquired intra-operatively. The depth of the insertion hole can be measured using a standard depth gauge. After a screw is inserted, X-ray images are typically acquired to confirm its correct placement. When all the fixation screws are in place, confirmation X-ray images may be required. An overview of the treatment of distal radius fracture by means of ORIF can be found in [10, 26, 29]. Even though ORIF is a widely used procedure, it is still quite challenging to estimate the length and the position of the fixation screws under fluoroscopic control.

Several studies report that the irregular anatomy of the distal radius leads to unrecognized cortical perforation by screw tips, independently of the art of locking plating: dorsal, palmar, or volar [2, 30]. Sugun et al. [30] reported a screw prominence rate of 25.65%, ranging from 0.5 to 6.1 mm. Depending on the type of the employed view (lateral, anterior-posterior, supinated, pronated, etc.) protrusions ranging from 3 to 6.5 mm on average must occur before they can be detected. It was also suggested that screw prominence greater than 1.5 mm is likely to cause problems [30]. Aurora et al. reported that 9% of all complications are related to protruding screws [2], like tendon rupture or plunging the drill bit into undesired soft-tissue structures [12]. Typically, revision surgery and implant removal are advised at the first sign of tendon irritation. Post-operatively, the severity of the complications associated with prominent screws is known. An additional critical aspect is the damage caused by perforation of the articular compartments by the drill bit, while preparing the screw hole. In an extensive study conducted on cadaver forearms, Pichler et al. [25] reported a 43% incidence of drill bit violation of the third extensor compartment.

This leads to: 1) a trial-and-error process during the surgery for correct drilling and screw positioning; and 2) empty drill traces injuring soft tissue compartments [1]. Hence, clinical practice advocates for better intra-operative position control. Researchers continue investigating guidance techniques for orthopedic and trauma procedures. Although the use of navigation solutions can increase the procedure time, or involve a learning curve, such systems increase accuracy and reduce inter-user variability [11]. Commercial solutions like Vector Vision (Brain Lab) make use of infrared stereo-cameras and related markers. Two more recently proposed approaches [6, 13] are based on the use of robotics or of an augmented mobile C-arm. All these initiatives involve additional dedicated hardware inside the operating room. In the same spirit, Egli et

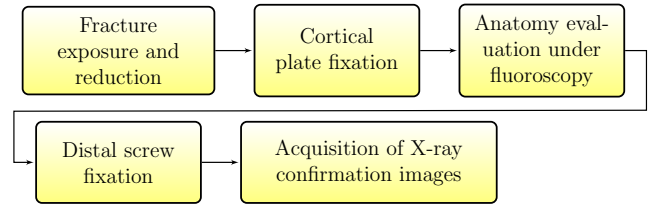


Fig. 1 Standard ORIF’s workflow at the distal radius.

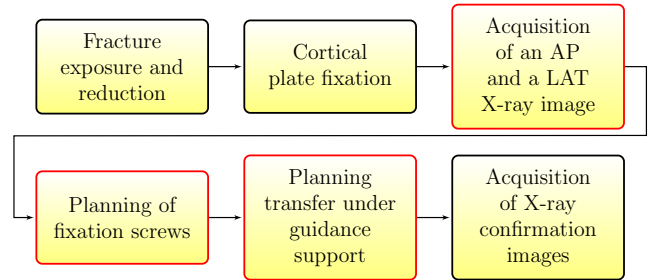


Fig. 2 Proposed workflow for an ORIF procedure at the distal radius. The procedure steps, at which our UPG framework explicitly supports the surgeon are marked in red.

al. [7] presented an intra-operative planning approach, i.e. the planning of the screw length and orientation is done directly in the operative room and not before. This technique was clinically evaluated by Vetter et al. [32] and Franke et al. [9]. However, its focus was solely on the intra-operative planning, leaving the task of applying the screw plan to the surgeon without further support. A combination of intra-operative planning and guidance would help reduce the screw placement errors and the number of cycles for each screw, including confirmation of the drilling trajectory, depth measurement, screw insertion and confirmation of the final position.

We present a Unified-Planning-and-Guidance (UPG) framework for fracture reduction and fixation applied to distal radius surgery. Our framework (see Fig. 2) introduces minimal alterations into the standard clinical workflow. After the plate has been fixed onto the bone shaft, our UPG scheme supports the physician in deciding the screw length and orientation through an augmented view of the implant plate onto intra-operative X-rays. The core of our system is the translation of the planning in local screw plans. A local screw plan is a plan for a screw’s length and orientation expressed in the local coordinate system of the corresponding screw hole. The current instrument position and its offset from the planned trajectory are visualized w.r.t. the implant plate and the patient anatomy. Guidance during drilling is provided solely by a combination of local markers observed by a camera mounted on the surgical drill. Our guidance:

1) provides real-time feedback of the tip position and of the orientation of the drill bit; 2) does not entail radiation exposure; and 3) does not constrain the movement of the medical personnel around the operating table.

This paper is an extension of the work presented in [18]. Novel contributions include: 1) the presentation of the design of the user interface of our guidance module; 2) the description of the developed algorithms for marker design and detection; 3) preliminary testing performed on fractured forearm specimens (AO A2 type); 4) evaluation of the accuracy of the real-time feedback of the position of the drill bit during the procedure using our custom-made marker reference; 5) investigation of the difference in screw-placement accuracy through our framework, compared to freehand drilling.

This paper is organized as follows: we first describe the hardware components of our design, and present our marker design and the algorithms developed for marker detection. Afterwards, we provide a detailed description of our modules for intra-operative planning and guidance. We then present our experimental setup, followed by the obtained results and relative discussion.

2 Methods

Pre-operatively an assessment of the fracture is performed. The status of the soft tissue is assessed and the injury is examined using X-rays radiographies. Displaced fragments, fracture extent, articulation involvement and quality of the bone are evaluated. The fracture is then classified (using e.g. the AO classification), which helps decision-making for the type of treatment. The surgeon may also decide to acquire radiographs of the uninjured forearm for comparison. Depending on the patient's and injury's conditions, the surgery may be performed right after injury or 5 to 6 days later [10].

Intra-operatively our UPG framework for fracture reduction supports the surgeon both during the planning of the fixation screws and during the planning transfer, i.e. while drilling for the preparation of the pilot hole according to the planned trajectory. After the repositioning of the fracture, the surgeon is asked to acquire two X-ray images: a lateral image, I_{LAT} , and an anterior-posterior image, I_{AP} (1st red box in Fig. 2). According to the standard clinical workflow, at this stage the implant is fixed to the shaft of the radius, by means of one or more cortical screws. An automatic 2D/3D gradient-based registration [7] allows the registration of the model of the implant plate to I_{LAT} and I_{AP} . After the registration, the plate is visualized on both X-ray images (see Fig. 3). The resulting augmented view is used by the physician to determine the number of the

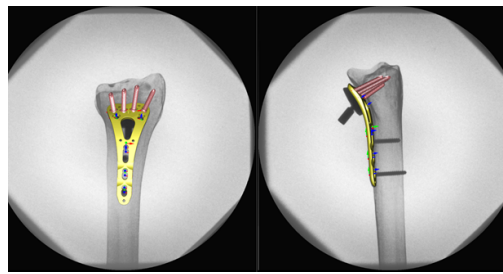


Fig. 3 Example of an intra-operative plan, which was performed on a plastic bone during our experiments.

fixation screws and their length (2nd red box in Fig. 2). The planned parameters are also visualized w.r.t. the surface of a variable angle drill-sleeve. While drilling, the drill sleeve is positioned onto the implant hole, for which the insertion hole needs to be prepared. In the work of Egli et al. [7], no further support was provided during the planning transfer, which was solely performed freehand. Confirmation of the depth and direction of drilling still required fluoroscopic images.

As we described in [18], we integrate our compact guidance solution [16, 17] with the planning module of Egli et al. [7, 9, 32]. Our method provides real-time guidance during screw positioning using minimal additional instrumentation (3rd red box in Fig. 2). In comparison to standard navigation solutions, we do not require the fixation of any reference markers onto the patient. Instead, our UPG framework provides position feedback by augmenting standard surgical instrumentation i.e., a surgical drill sleeve and the surgical drill, with optical markers and a small video camera respectively. While drilling, the markers are imaged by the video camera rigidly fixed onto the drill. The position of the drill bit w.r.t. the drill sleeve is then computed using the geometric relations between the features of the markers, which are detected in the camera images, and their respective physical coordinates. The drill bit position can then be expressed w.r.t. the implant plate. The registration of the implant plate allows us to visualize the tip and the direction of the drill bit onto the X-ray images.

In the following subsections, we present for the first time our revised marker design and the algorithms, for detecting and identifying in real-time the markers in the camera images. We also describe how we identify and subsequently reject from further processing highly blurred images, which are acquired during drilling.

2.1 Marker Design

In our application, space constraints strongly limit the admissible number of markers onto the surgical drill sleeve [16]. Our configuration consists of 3 non-coplanar

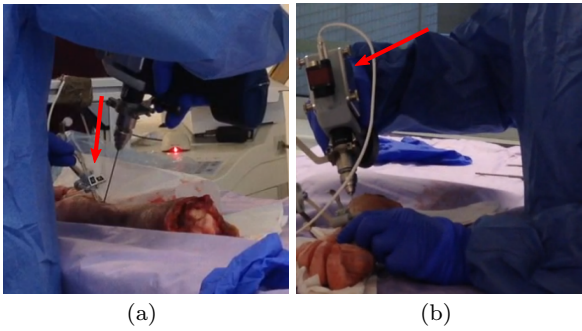


Fig. 4 Our hardware design: (a) the drill guide with attached markers and (b) the drill with the mounted camera.

markers (see Fig. 5(a)). In our current design, the marker size is 8×8 mm. Each marker is overlaid onto a white surface, for better contrast, resulting in a total size of 12×12 mm. The marker base is 2 mm thick. We found that this marker size was small enough not to interfere with the stable positioning of the drill sleeve onto the implant plate. The minimum bounding volume for our marker configuration is about 6.3 cm^3 . In our previous work [16, 17], we determined that square and binary encoded markers perform best in our setup. Unlike [17], we adopted redundant binary encoding to increase the robustness of marker identification.

Extensive work can be found in the literature on marker encoding, where not only the ID of the marker is encoded, but also a redundant part [8, 24, 33]. This allows for the detection of errors in the read-out of the ID, as well as their correction up to a maximum number t . Remarkable performances, in terms of robustness, have been reported by the AprilTag [24] system and the incorporation of BCH (Bose-Chaudhuri-Hocquenghem) codes [4] into ARToolKitPlus [33]. Due to the aforementioned physical space constraints, we are only interested in a small number of markers. However, the code correction capability of BCH encoding is a valuable attribute. In our marker design, the marker IDs are 5 bits encoded. The ID is repeated three times inside the marker, two times as a BCH code and once as clear ID, i.e. without any redundant part. The use of a 3-times repetition scheme is a known technique in coding theory [23]. We adopted the BCH(15,7,2) encoding scheme. The codeword $c(x)$ is 15 bits long: 7 bits for encoding the marker ID and 8 for the redundant part, which is used for error detection and correction. Five bits out of the 7 encode our ID, while the remaining 2 bits are reserved and set to “11”. Due to the low number of bits in our design, we use a look-up table for faster decoding [3, 5, 19, 34]. BCH codes can not recover from burst errors of more than t bits. If before the correction one or both reserved

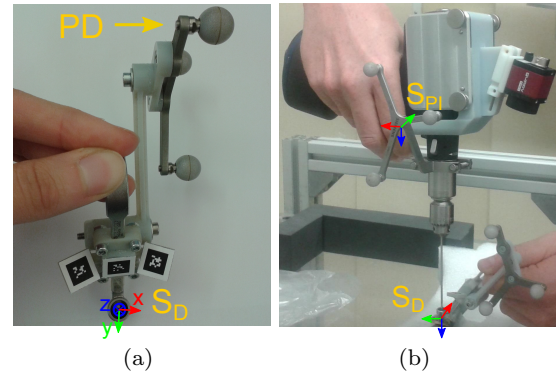


Fig. 5 (a) The drill sleeve with our attached markers. Our custom-made marker holder has an extension to rigidly fix the Polaris markers, which were used for reference data measurement. (b) The surgical drill used in our experiments.

bits are different from 11 and they do not get corrected, we can not trust the correction we made.

2.2 Marker Detection

Our marker detection algorithm is designed to address some of the issues related to our application, e.g. varying illumination and partial marker occlusion. Under such conditions, edge-based algorithms are shown to perform robustly [8, 24]. Unlike our previous work [17], which used image thresholding and corner detection, we now base our algorithm on edge detection.

First, a Sobel operator is applied to estimate the image gradient, $\mathbf{G} = (G_x, G_y)$. To simplify the detection of the marker boundaries, we first detect straight edge segments and classify them in 4 classes according to the direction of their \mathbf{G} . We identify vertical, v_V and horizontal edges, v_H : v_H are then subdivided in $G_y \geq 0$, labeled as “green” and $G_y < 0$ labeled as “blue”; v_V in $G_x \geq 0$, labeled as “red”, and $G_x < 0$, labeled as “purple” (see Alg 1). An example of color-coded edges is shown in Fig. 6. Since our markers are designed with a black interior and a white border, the vector \mathbf{G} at the borders always points away from the marker’s center. The sequence of the edges at the marker boundaries is: green, purple, blue and red. The search for each edge type can be processed in parallel. A 16-bit ID is assigned to each edge segment (see Fig. 7). An ordered 64-bit ID is built for each candidate marker. Multiple detections of the same candidate can be easily avoided, rejecting quads whose ID already exist. The steps for the quad formation are shown in Alg. 2.

Each marker has a unique pattern of white and black subsquares. Identifying a marker is then equivalent to identifying the marker ID (see Sec. 2.1), which is associated with the specific sequence of subsquares. A

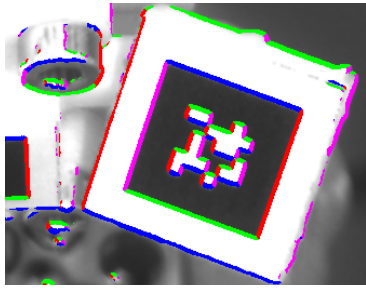


Fig. 6 The 4 type of edge classes are shown.

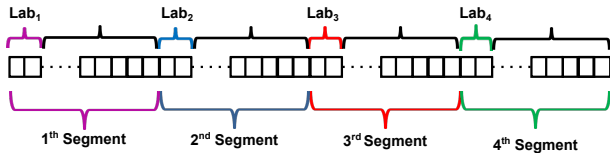


Fig. 7 The encoding of the 4 edge segments forming a candidate marker. Two bits encode the color label, Lab_i , of the class to which the segment belongs. The remaining 14 bits encode the unique ID of the segment inside its respective class.

threshold is calculated for each candidate marker by averaging the pixels' intensities at its border. Then the inner region is thresholded. Each subsquare is assigned the value 1 or 0. Hence, a binary sequence is read-out and the candidate ID is extracted. The corner locations of all the valid markers are then used to recover the position of the drill bit using the algorithm of Lu et al. [15] or the algorithm of Schweighofer et al. [28] if just one marker is detected as in [33].

2.3 Identification of Highly Blurred Images

In our previous work [17], we observed that when the drill bit perforates the bone or hits the drill sleeve, the acquired images are heavily blurred. As in [18], to avoid processing such images, we use a blur measure to identify and reject this type of images.

We used a no-reference blur metric inspired by the work of Marziliano et al. [21], which is based on the calculation of the average edge spread in the spatial domain. On each row r_i , the local extrema around each edge point are identified and their distance d_{Ei} is treated as the local spread of the edge. The blur metric b_x is then defined as the average over all edge spreads: $b_x = \frac{\sum_{i=1}^{N_x} d_{Ei}}{N_x}$. Unlike [21], we considered both vertical and horizontal edges. The final blur metric b is then obtained as the sum of the vertical (b_x) and horizontal (b_y) contributions: $b = b_x + b_y$. In Alg. 3, the steps for the calculation of b_y are described. Edge detection is already the first step of our marker detection algorithm. Hence, this metric does not significantly increase the computational cost. We calculate it only on ROIs

Alg 1: Edge segment grouping per edge class

Data: Gradient Images: $G_x(x,y)$, $G_y(x,y)$, and gradient magnitude image I_G ($W \times H$)
Result: 4 lists of labeled edge segments (l_g, l_p, l_b, l_r), one per class l_i : green/purple/blue/red
Initialize each l_i , In parallel;
for $y = 1 : H$ **do**
 for $x = 1 : W$ **do**
 read $G_x(x,y)$, read $G_y(x,y)$;
 determine class label l_i as follows;
 if $I_G(x,y) \in v_H$ **then**
 if $G_y(x,y) \geq 0$ **then**
 $I_G(x,y) \leftarrow l_g$
 else
 $I_G(x,y) \leftarrow l_b$
 if $I_G(x,y) \in v_V$ **then**
 if $G_x(x,y) \geq 0$ **then**
 $I_G(x,y) \leftarrow l_r$
 else
 $I_G(x,y) \leftarrow l_p$
 if $I_G(x,y)$ is 4-connected pixel and $\in l_i$ **then**
 $I_G(x,y) \leftarrow l_i$;
 for each segment s_i **in** l_i **do**
 $s_i \leftarrow$ 16-bit ID;
 calculate dir, start, end, mean gradient vector v_G ;

around the marker edges. A blur value $b \geq 47$ indicates a highly blurred image. The threshold value was empirically determined from a drilling video sequence.

3 Unified-Planning-and-Guidance

The main modules of our framework, which were introduced in [18], i.e. the module for the intra-operative planning and the module for intra-operative guidance, are described in detail in the following subsections. Furthermore, we present for the first time the combined use of the Kalman filter, which we employ to cope with missing marker detection. The details of the user interface of our guidance module are also presented.

3.1 Intra-operative Planning

According to the planning module of Egli et al. [7], which we integrated in our framework [18], after the implant plate has been fixed onto the bone shaft, the physician is asked to acquire two X-ray images: a lateral, I_{LAT} , and an anterior-posterior, I_{AP} . The X-ray images are intra-operatively acquired using a mobile C-arm. The implant plate model P_L is then registered to I_{LAT} and I_{AP} via an automatic 2D/3D registration [7]. The method developed by Egli et al. is based

Alg 2: Edge linking. The algorithm is started from each of the segment classes. The neighboring segment is searched for only in the compatible set according to the sequence: green (g), purple (p), blue (b) and red (r).

Data: 4 lists of labeled edge segments (l_g, l_p, l_b, l_r)
Result: List of markers: L_M
Initialize list of candidates markers L_Q ;
In parallel, starting at each $l_i \in \{l_g, l_p, l_b, l_r\}$ and selecting l_j, l_k, l_l based on the ordered sequence of colors;

```

for  $i = 1 : \text{size}(l_i)$  do
  Quad  $\leftarrow s_i \in l_i$ ;
  for  $j = 1 : \text{size}(l_j)$  do
    read  $s_j \in l_j$ ;
    if  $s_j$  is compatible with  $s_i$  then
      | Quad  $\leftarrow s_j$ ;
    for  $k = 1 : \text{size}(l_k)$  do
      read  $s_k \in l_k$ ;
      if  $s_k$  is compatible with  $s_j$  & Quad then
        | Quad  $\leftarrow s_k$ ;
    for  $l = 1 : \text{size}(l_l)$  do
      read  $s_l \in l_l$ ;
      if  $s_l$  is compatible with  $s_k$  & Quad then
        | Quad  $\leftarrow s_l$ ;
  ID(Quad)  $\leftarrow (\text{ID}(s_g), \text{ID}(s_p), \text{ID}(s_b), \text{ID}(s_r))$ ;
  if ID(Quad)  $\notin L_Q$  then
    |  $L_Q \leftarrow \text{Quad}$ ;
for each Quad  $Q_i$  in  $L_Q$  do
  T  $\leftarrow$  average intensity at the Quad's border;
  Quad's interior is thresholded using T;
  Marker(ID) is extracted;
  if Marker(ID) is valid then
    |  $L_M \leftarrow \text{Marker}$ ;

```

All the corner features $\in L_M$ are used for the drill's pose recovery;

on phase and gradient correlation similar to the work of Kreuder [14]. A radial basis function is used to approximate the cost function. A conjugate direction method is used to reach the optimal registration. The registration result is described by the transformation matrices \mathbf{T}_{LAT}^{PL} and \mathbf{T}_{AP}^{PL} . Once registered, the model of the plate is overlaid onto I_{LAT} and I_{AP} . The augmented views support the physician in deciding the number of screws, their length and their orientation. Each screw is also visualized together with the implant plate. The comprehensive augmented view (see Fig. 3) is available to the physician during the entire decision process.

The planned screw configuration is then expressed as a set $X = \{(\mathbf{p}_{T_i}, \mathbf{v}_{A_i})_{H_i}\}$, where $(\mathbf{p}_{T_i}, \mathbf{v}_{A_i})_{H_i}$ represent the screw tip position and the screw direction vector, respectively, expressed in the local coordinate system (CS) of the i -th hole, S_{H_i} , of the employed plate.

Alg 3: Edge spread calculation for the horizontal edges for a ROI defined around a marker.

Data: ROI ($w \times h$) of the gradient image
Result: Average edge spread b_y

```

for  $y = 1 : h$  do
  for  $x = 1 : w$  do
    read ROI( $x, y$ );
    if ROI( $x, y$ ) is a horizontal edge pixel then
      find gradient trend  $t_g$  on the rows above;
      if  $t_g$  is increasing then
        |  $y_S \leftarrow$  find local maximum;
      else
        |  $y_S \leftarrow$  find local minimum;
      end
      find gradient trend  $t_g$  on the rows below;
      if  $t_g$  is increasing then
        |  $y_E \leftarrow$  find local maximum;
      else
        |  $y_E \leftarrow$  find local minimum;
      end
       $b_{y_i} \leftarrow y_E - y_S$ 
    end
  end
end
 $b_y \leftarrow$  average of all  $b_{y_i}$ 

```

3.2 Intra-operative Guidance

The plate registration and the parametrization of the planning in terms of the set of local screw coordinates X allow the guidance pipeline to be decoupled from a global patient reference [18], as traditional navigation systems would require. As part of our design, a standard surgical drill sleeve is augmented with a holder, onto which we place our binary encoded markers (see Fig. 5(a)). A small video camera (Allied Vision Technologies, Guppy Pro F-125 BW, 1024×768) is mounted onto a standard surgical drill.

The relative transformation between the camera S_C , S_C , and the drill bit is determined via a one-time calibration procedure, which is performed when the camera is attached to the drill, and is represented by \mathbf{T}_C^I [17]. The core calibration step takes about 3mins. Together with a visual confirmation for a thorough calibration, the entire procedure takes on average 30mins.

Before drilling, the physician is asked to position the set of drill-sleeve markers, S_D , onto the implant plate, as depicted in Fig. 9(a). Thus, S_D does coincide with the local CS of the current hole S_{H_i} . While drilling, the markers on the drill sleeve are inside the Field of View (FoV) of the camera. Marker detection and subsequent camera pose estimation, expressed by \mathbf{T}_D^C , are performed in real-time. The geometric relations between an implant plate hole, S_{H_i} , the set of drill-sleeve markers, S_D , the camera, S_C , and the drill bit, S_I , allow

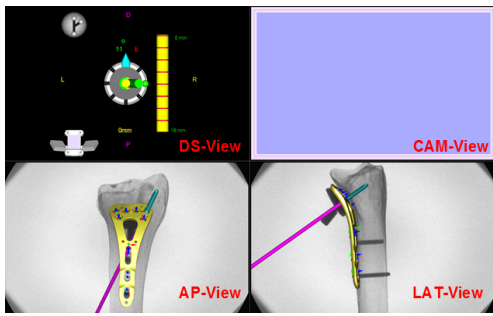


Fig. 8 UPG user interface for the guidance module.

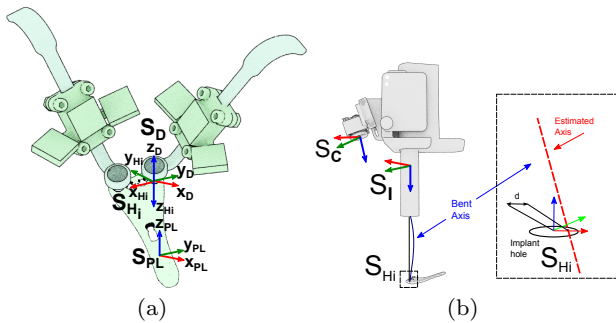


Fig. 9 (a) A schematic representation of our augmented drill guide positioned on an implant plate. (b) Graphic depiction of the problem of the axis offset due to axis bending.

us to calculate the transformation $\mathbf{T}_{H_i}^I$, from S_I to S_{H_i} :

$$\mathbf{T}_{H_i}^I = \mathbf{T}_{H_i}^D \mathbf{T}_D^C \mathbf{T}_C^I \quad (1)$$

We then estimate the position of the drill-bit w.r.t. S_{H_i} as $(\mathbf{p}_I, \mathbf{v}_I)_{H_i}$. The transformation $\mathbf{T}_{H_i}^D$ depends on the selected orientation of the drill sleeve and is known by construction; $\mathbf{T}_{P_L}^{H_i}$ is also known by construction.

The previously performed 2D/3D registration between the implant plate and the intra-operative X-rays allows us to report the instrument position directly onto I_{AP} (the final transformation, \mathbf{T}_{AP}^I , in Eq. 2) and I_{LAT} .

$$\mathbf{T}_{AP}^I = \mathbf{T}_{AP}^{P_L} \mathbf{T}_{P_L}^{H_i} \mathbf{T}_{H_i}^I \quad (2)$$

Our framework allows us to calculate the instrument position in real-time at an average frame rate of 15 Hz.

During the planning transfer, the user is advised to follow the natural sequence of 2 steps: 1) Targeting and 2) Drilling.

3.2.1 Combined use of the Kalman Filter

In our real-time drill guidance, the instrument position is calculated for each camera frame. However, if no markers are detected, e.g. the markers are outside the FoV of the camera, the position of the instrument can not be calculated. Moreover, the vibrations of the

instrument, as well as strong illumination changes negatively affect the outcome of the marker detection, both in terms of the number of the detected markers and of the accuracy of the detected features. Our goal is to provide continuous position feedback and avoid annoying interruptions in the instrument visualization.

To provide an estimate of the drill bit position, even in the absence of detected markers, we use a linear Kalman filter. For more details on the Kalman filtering method see [31]. Our state vector \mathbf{x} (see Eq. 3) and the transition matrix \mathbf{A} (see Eq. 5) are modeled as described in Zhao et al. [35]. The direction vector of the instrument axis is described by the azimuth and elevation angles, ϕ and θ . Hence, $\mathbf{v}_A = [\phi, \theta]^T$ and $\omega_A = [\omega_\phi, \omega_\theta]^T$ represent the orientation and the angular velocity of the instrument axis, and $\mathbf{p}_{T_i} = [x_T, y_T, z_T]^T$ and $\mathbf{v}_P^T = [v_x, v_y, v_z]^T$ denote the position and the velocity vector of the instrument tip respectively. Unlike Zhao et al. [35], the velocity components can not be provided by a second measurement device. Instead, we calculate both the tip velocity, $\mathbf{z}_{v_p}^T$, and the angular velocities, $\mathbf{z}_{\omega_A}^T$, as the difference between the position measurements of two consecutive frames. Our measurement vector is defined as in Eq. 4. The measurement matrix is $\mathbf{H} = \mathbf{I}_{10 \times 10}$. Since the drill is manually steered, no control input is included in the model.

$$\mathbf{x} = [\mathbf{v}_A^T, \omega_A^T, \mathbf{p}^T, \mathbf{v}_P^T]^T \quad (3)$$

$$\mathbf{z} = [\mathbf{z}_{v_A}^T, \mathbf{z}_{\omega_A}^T, \mathbf{z}_{p_T}^T, \mathbf{z}_{v_p}^T]^T \quad (4)$$

$$\mathbf{A} = \begin{bmatrix} \mathbf{I}_{2 \times 2} & \mathbf{I}_{2 \times 2} & \mathbf{0}_{2 \times 6} \\ \mathbf{0}_{2 \times 2} & \mathbf{I}_{2 \times 2} & \mathbf{0}_{2 \times 6} \\ \mathbf{0}_{3 \times 4} & \mathbf{I}_{3 \times 3} & \mathbf{I}_{3 \times 3} \\ \mathbf{0}_{3 \times 4} & \mathbf{0}_{3 \times 3} & \mathbf{I}_{3 \times 3} \end{bmatrix} \quad (5)$$

The Kalman filter is updated at each frame. However, its extracted values are used only as needed. Moreover, tracking is constrained in time to prevent the filter from diverging from the real position of the drill, which is manually steered. Hence, tracking is allowed for a maximum of $N_f = 4$ frames. If no markers are detected after N_f frames, we stop updating the instrument position on the screen. As soon as markers are detected, the Kalman filter is re-initialized. The position delivered by the filter is also used when the angular difference of the drill axis between two consecutive frames is greater than 10° . In these cases, the predicted drill position, as described by \mathbf{x} , is used for the calculation of the velocity component of the successive frame.

3.3 Instrument Visualization

Four different views are used for visualization (see Fig. 8). The position of the drill bit is visualized in

real-time onto both I_{LAT} and I_{AP} . These views allow: a) the visualization of the position of the instrument w.r.t. the patient anatomy and b) the verification of the quality of the instrument calibration. By pointing the tip of the drill bit at a notable position of the plate, the quality of the correspondence, between the real position of the drill bit and the visualized one, can be visually inspected on the fly at any time during guidance.

The drill bit position is also shown on a comprehensive view, DS-view, at the top of the guidance window (see Fig. 8). In the DS-view, the planned and the current direction of the screw axis are displayed w.r.t. the drill sleeve to the surgeon. By reflecting the real physical situation at the corresponding screw hole at the moment of drilling, this simple and local view of the instrument direction allows the surgeon to concentrate on the parameters of the current screw.

In the DS-view, the depth of the drill bit is visualized using a depth indicator. The planned length of the screw is also shown next to the depth indicator. The depth of insertion, d_s , is calculated as the difference between the planned screw length l and the distance to the target. We first consider the planned screw direction and the planned screw-tip position at the selected screw-hole: $s_i = (\mathbf{p}_{TH_i}, \mathbf{v}_{AH_i})$. We then consider the plane π_s , orthogonal to the screw direction and passing through the screw. While drilling, we calculate the perpendicular distance, d_p , between the calculated tip position, $\mathbf{p}_T = (x_{pT}, y_{pT}, z_{pT})$, and π_s . The depth of insertion d_s , is determined as $d_s = l - d_p$.

To calculate the drill bit position, the markers on the drill sleeve need to be in the FoV of the camera. The information about the marker visibility is presented to the surgeon in 2 of the 4 views (see Fig. 8). On the upper right viewport, CAM-view, the video stream of the camera is shown in real-time. The visibility of the markers is conveyed in the DS-view via a 3D mesh of the marker holder displayed in the bottom left corner of the viewport. The marker holder is colored green, yellow, red or gray, if 3, 2, 1 or 0 markers are visible, respectively. During our tests, the physician used both viewports. The CAM-view was used to optimally rotate the drill towards the markers. During targeting and drilling, the surgeon focused on the DS-view and relied on the visibility information provided by the color of the marker model. By clicking on the CAM-view, the camera images could be hidden or visualized on demand.

Before drilling, our guidance module offers the surgeon the possibility to change the orientation of the drill sleeve w.r.t. the implant hole (see Fig. 9(a)). The default configuration assumes that the drill sleeve is positioned with its handle oriented towards the distal side

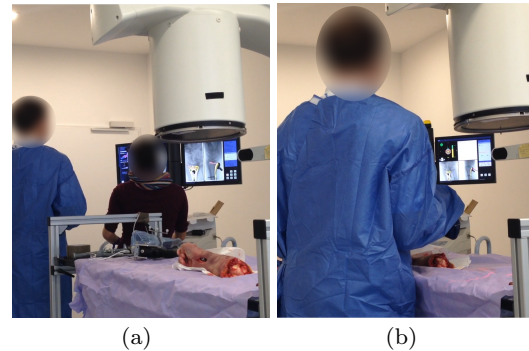


Fig. 10 Pictures taken during our experiments: (a) planning phase and (b) the guidance phase.

of the radius. If the user desires to position the drill sleeve in one of the other available orientations, the chosen one has to be provided to the software before drilling. A change in the orientation of the drill sleeve may be desirable in order to limit the contact between the drill sleeve and the surrounding tissues.

Depending on the diameter and the length of the drill bit, bending of the drill bit can occur during the operation. However, our instrument calibration is expressed by the rigid transformation \mathbf{T}_C^I . The tip position and the axis direction can be obtained only indirectly. A bending of the drill bit undermines our rigidity assumption (see Fig. 9(b)) and can lead to the display of a false offset of the drill bit position. Using sensors (e.g. electromagnetic sensors) directly on the tip would help reduce the risk of false position information [27]. Unfortunately, these solutions can not be applied in our case. As with all hand-held instruments, no knowledge of the kinematics of the drill bit is available. Hence, no modeling for the drill bit bending can be applied.

Safety concerns require the recognition of this critical case. Note that the drill bit trajectory is constrained to pass through the origin \mathbf{O}_{H_i} of S_{H_i} . Thus, we calculate the intersection \mathbf{p}_{A_i} between the estimated drill bit trajectory and the plane orthogonal to the hole axis. Values of the distance d between \mathbf{O}_{H_i} and \mathbf{p}_{A_i} other than 0 are considered as an indication of drill bit bending. A warning is given to the user, in the form of a color change of the drill sleeve in the DS-view, suggesting that attention should be paid while holding the drill. Different colors are used depending on the value of d . To obtain an estimate of the possible tip offset, we considered an axis bending on a single plane starting at the midpoint (\mathbf{m}) of the drill bit. We have empirically determined that if the angle described by the base of the drill bit and \mathbf{m} before and after deformation is 5° , the displayed offset could be up to 15 mm.

4 Experiments

To evaluate the accuracy in the screw placement, which can be achieved using our UPG framework, an extensive series of experiments was conducted on distal radius bone phantoms and on forearm cadaver specimens. Preliminary results on the bone phantoms and healthy forearm specimens were presented in [18]. Here, we extend our analysis to initial testing on fractured forearm specimens. We also investigate the impact of our UPG framework on the accuracy of the screw placement as compared to the freehand approach. We also analyze the accuracy of the real-time position feedback of the drill bit delivered by our camera-drill system.

In our experiments, a total of 37 (16 rights and 21 left) bone phantoms (involving 147 screws) were operated. Further experiments were conducted on 3 healthy forearm specimens (2 rights and 1 left involving 11 screws for which the drill sleeve was correctly oriented) and on 2 forearm specimens (involving 8 screws), for which an AO A2 type fracture was produced by the operating surgeon using a drill with a saw attachment. The length of the placed screws (2.4 mm variable angle locking screws, Synthes Inc.) ranged from 14 to 24 mm. The plate used in all the experiments was a standard 2.4 mm Variable Angle LCP Two-Column Volar Distal Radius Plate, with a 6-hole head (Synthes Inc.). A standard drill bit \varnothing 1.8 mm, with marking, length 110 mm, 2-flute (Synthes Inc.) was used, as well as a battery-powered drill, Colibri II (Synthes Inc.). Two user groups (4 users with engineering expertise, EE, and 2 medical experts, ME) operated on the phantoms. The specimens were operated by one medical expert. According to our workflow, for each test the operator was asked to: 1) fix the implant to the test-body; 2) acquire 2 radiographic images for implant registration; 3) plan the desired screw configuration; 4) select the current screw hole and accordingly position our marker-drill sleeve; 5) transfer the plan, guided by the real-time feedback of our software; and 6) place the screws and acquire a 3D volume (Arcadis® Orbic 3D, Siemens; Volume: 256³; Spacing: 0.485 mm).

Evaluation of the transferred plan: Following the evaluation procedure used by Vetter et al. [32], at the end of each test case, the implant plate is manually registered to the acquired 3D volume. This allows us to evaluate the accuracy of the transferred plan in terms of: 1) the Euclidean distance between the planned and the achieved position of the screw tip, d_T ; and 2) the difference between the planned and realized screw axis orientation, expressed in azimuth, α , elevation, β , using the convention of Vetter et al. [32], and total angle, ψ (see Table 1). Our error estimates depict the overall

accuracy of the entire process. The use of the azimuth and elevation angles allows us to compare our results with those of [32]. Furthermore, the use of two separate angles provides us feedback on whether certain screw orientations are more error-prone (see Fig. 16).

Evaluation of the real-time position feedback of the drill bit: We also assessed the accuracy of the position feedback delivered by our system by using a Polaris tracking system (NDI, Ontario, Canada) for reference data collection. We compared the instrument position, calculated in real-time by our guidance application (15 Hz) on the 37 PB and on the 5 FS, with the one obtained by the Polaris (20 Hz). Recall that our framework expresses the position of the drill bit w.r.t. the local CS of the drill sleeve, S_D , as $(\mathbf{P}_{IC}, \mathbf{v}_{IC})_D$. Hence, we attached Polaris reflective markers to both the drill sleeve and to the surgical drill. This allowed us to express the position of the drill bit, given by the Polaris system, in terms of S_D , as $(\mathbf{P}_{IP}, \mathbf{v}_{IP})_D$. For each screw, the data was acquired during the entire guidance procedure, including drill positioning, targeting, drilling, position readjustment and calibration check.

UPG framework vs. freehand placement: The 4 users of the EE group were each asked to transfer a set of 5 screw plans twice on PB: once freehand, and once under the feedback provided by our UPG framework. Each user was assigned a different set of screw plans. User #4 operated on only 3 screw plans.

4.1 Drill Sleeve Calibration

For comparison with our Polaris-based reference, we need to calibrate both the drill and the drill sleeve with the attached Polaris markers. Our drill-Polaris marker calibration is expressed by the transformation \mathbf{T}_{CP}^I , where CP is the Polaris reference attached to the drill.

For the drill sleeve calibration, we designed a custom made calibration plate (see Fig.11). For maximum flexibility, S_D is used as reference frame. Polaris markers are attached to the plate K. The implant plate, PL, is rigidly fixed onto the plate and the transformation \mathbf{T}_{PL}^K , from K to PL is known by construction. Recall that when the drill sleeve is fixed onto one of the implant holes, S_D is expected to coincide with the local hole S_{H_i} . The transformation matrix $\mathbf{T}_{H_i}^{PL}$ from PL to the plate hole H_i is also known. Our sought calibration is expressed by \mathbf{T}_D^{DP} , which can be obtained using Eq. 6. In Eq. 6, only \mathbf{T}_K^{DP} is missing. Hence, we placed the drill sleeve onto the two central distal holes of the implant, one after another, obtaining a pair of estimates of $\widehat{\mathbf{T}}_P^{DP}$, which we averaged to get our final estimation of \mathbf{T}_P^{DP} .

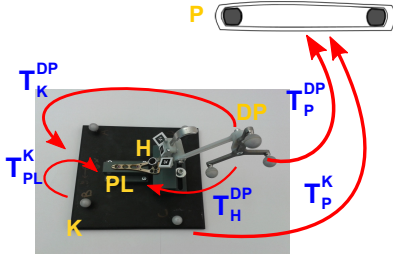


Fig. 11 Our custom-made calibration plate for the calibration of the drill sleeve with attached Polaris markers, S_{DP} .

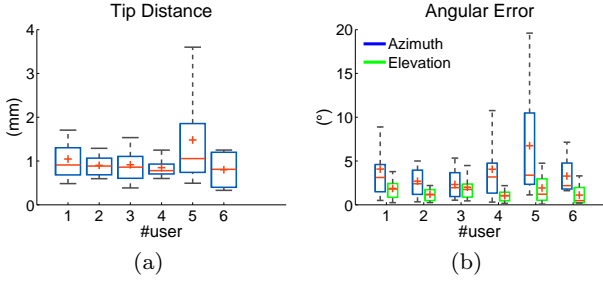


Fig. 12 Inter-user variability in the screw placement for the plastic bones for (a) the tip error, and (b) the angular error in azimuth (blue) and elevation (green). Engineering experts are users #1 to #4 while medical experts are users #5 and #6. User #6 operated on a single phantom.

$$\mathbf{T}_D^{DP} = \mathbf{T}_{H_i}^{DP} = \mathbf{T}_{H_i}^{PL} \mathbf{T}_{PL}^K \mathbf{T}_K^{DP} \quad (6)$$

To determine \mathbf{T}_K^{DP} , we placed our drill sleeve onto the implant and acquired data for about 10 sec. at 20Hz using the standard NDI Track Tool for a total of n measurements. Hence, we got a set of transformations $S_P = \{(\mathbf{q}_i, \mathbf{t}_i)\}$. The rotation component is expressed by the quaternion $\mathbf{q}_i = (q_W, q_X, q_Y, q_Z)$. The quaternion representation allows a straightforward averaging operation. We compute the average rotation component of \mathbf{T}_D^{DP} using the method proposed by Markley et al. [20]. As weights we used the error delivered by the NDI Track system when calculating \mathbf{T}_P^{DP} and \mathbf{T}_P^K .

5 Results

The obtained final accuracy in the screw placement on PBs and FSs is shown in Table 1. A fourth healthy specimen was excluded from the quantitative evaluation, since plate rotation occurred during the procedure. In Fig. 16, the error distribution w.r.t the planned screw direction is shown, both for azimuth, α , and elevation, β . Our ANOVA analysis showed significant ($p < 0.05$) difference in d_T and no significant difference ($p > 0.05$) in ψ between the two user groups, EE and ME. The performance of each user on PBs is shown in Fig. 12.

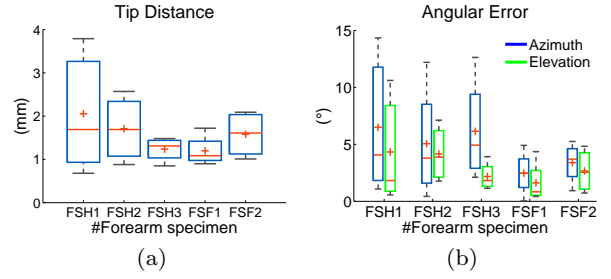


Fig. 13 Final accuracy in the screw placement for the forearm specimens: errors in (a) tip position, (b) azimuth and elevation angles. FSH1 to FSH3 and FSF1 to FSF2 denote the healthy and fractured forearm specimens respectively.

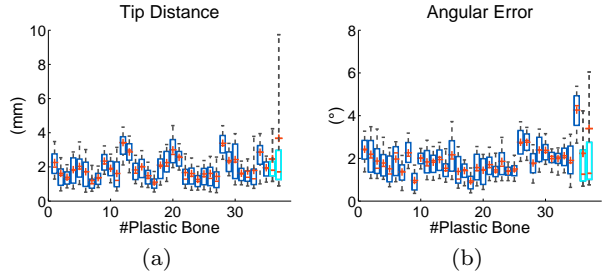


Fig. 14 Accuracy of the position feedback delivered by our camera-drill system in (a) tip distance and (b) total angle, for all the plastic bones PB. The last 2 PBs were drilled using a light-weight non-surgical drill.

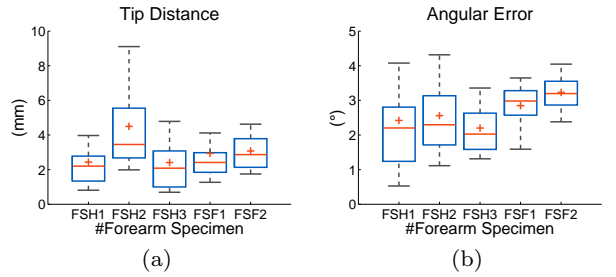


Fig. 15 Accuracy of the position feedback delivered by our camera-drill system in (a) tip distance and (b) total angle, for all the forearm specimens.

The final accuracy in the screw placement obtained on FSs is shown in Fig. 13. More specifically, the errors obtained for the 3 healthy specimens, FSH, in d_T , α and β are 1.63 ± 0.91 mm, $5.85 \pm 4.93^\circ$ and $3.48 \pm 3.07^\circ$ respectively [18]. The errors for the 2 forearm specimens with fractures, FSF, are 1.39 ± 0.47 mm, $2.93 \pm 1.83^\circ$ and $2.14 \pm 1.84^\circ$ respectively (see Table 1).

Fig. 18 shows the final screw accuracy, when a user transfers the same set of screw plans on PB, once free-hand, and once guided by our UPG framework. When transferring the same plan under guidance we achieved: 0.89 ± 0.37 mm, $2.85 \pm 2.57^\circ$, $1.49 \pm 1.17^\circ$ in d_T , α and β , compared to freehand: 1.73 ± 0.82 mm, $6.01 \pm 4.94^\circ$,

Table 1 Final accuracy in the screw placement. Mean and median values for tip distance (d_T), and for errors in azimuth (α), elevation (β) and total (ψ) angles for plastic bones: 1) All users (AU), 16 right bones (64 screws) and 21 left bones (83 screws); 2) Engineering experts (EE), 14 right bones (56 screws) and 19 left bones (75 screws); 3) Medical experts, (ME) 2 right bones (8 screws) and 2 left bones (8 screws). The last rows refer to the forearm specimens: all forearm specimens (FS, 19 screws), healthy (FSH, 11 screws) and with fractures (FSF, 8 screws) respectively.

	d_T (mm)		α ($^\circ$)		β ($^\circ$)		ψ ($^\circ$)	
	Mean	Median	Mean	Median	Mean	Median	Mean	Median
AU	1.01 ± 0.56	0.89	3.74 ± 4.39	2.64	1.70 ± 1.35	1.41	2.48 ± 1.58	2.18
EE	0.97 ± 0.46	0.89	3.48 ± 4.08	2.60	1.68 ± 1.30	1.46	2.39 ± 1.34	2.17
ME	1.34 ± 1.02	1.06	5.86 ± 6.18	3.18	1.85 ± 1.73	1.21	3.21 ± 2.87	2.39
FS	1.53 ± 0.75	1.27	4.62 ± 4.12	3.69	2.92 ± 2.65	1.82	3.75 ± 2.51	3.48
FSH	1.63 ± 0.91	1.40	5.85 ± 4.93	4.07	3.48 ± 3.07	2.17	4.54 ± 2.77	4.37
FSF	1.39 ± 0.47	1.18	2.93 ± 1.83	2.98	2.14 ± 1.84	1.22	2.67 ± 1.70	1.77

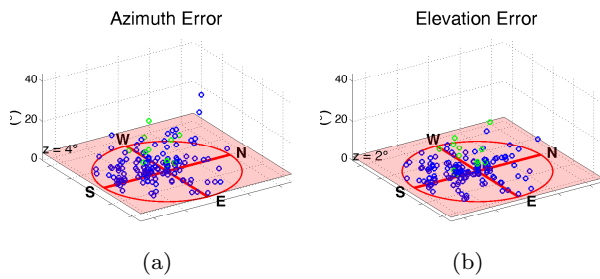


Fig. 16 Error distribution for the 4 angular sectors for PBs (blue), FSH and FSF (green), in: (a) azimuth and (b) elevation. North relates to the distal side of the plate.

Table 2 Accuracy of the position feedback of the drill bit. Mean and median values for the errors in the tip distance (d_{TG}), and the total angle (ψ_G) for: 1) All plastic bones (PB) for all users (AU), (147 screws); 2) All forearm specimens (FS) (20 screws). The results obtained when 1 marker (1M), 2 markers (2M) or 3 markers (3M) are detected are shown.

	d_{TG} (mm)		ψ_G ($^\circ$)	
	Mean	Median	Mean	Median
PB (AU)	2.01 ± 1.57	1.75	1.93 ± 1.35	1.83
1 M (9.93%)	2.53 ± 2.69	2.05	1.67 ± 3.13	1.25
2 M (27.71%)	2.19 ± 1.30	1.96	2.06 ± 1.07	2.02
3 M (63.36%)	1.84 ± 1.37	1.59	1.91 ± 0.82	1.86
FS	2.84 ± 2.48	2.41	2.70 ± 1.86	2.81
1 M (14.95%)	2.97 ± 3.13	2.48	2.02 ± 3.09	1.83
2 M (29.35%)	2.48 ± 2.53	1.98	2.39 ± 2.11	2.39
3 M (55.69%)	2.99 ± 2.21	2.59	3.06 ± 0.90	3.07

$3.52 \pm 2.48^\circ$. Our ANOVA analysis showed that there was a significant ($p < 0.05$) difference in d_T and in ψ between the two groups.

The overall accuracy of the real-time position feedback of the drill bit, as provided by our guidance module is shown in Table 2. The accuracy of the position feedback is expressed in tip distance d_{TG} and total angle ψ_G and was calculated over 147 drilling sequences for PB and 20 sequences for FS. The obtained accuracy for PBs and for FSs is shown in Fig. 14 and Fig. 15.

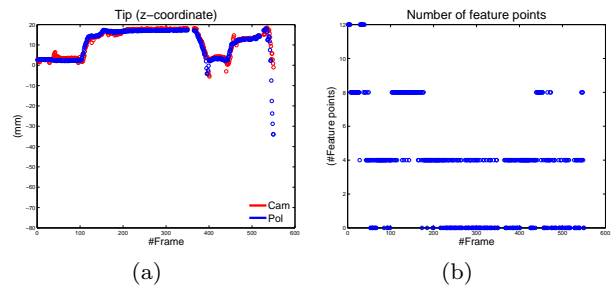


Fig. 17 Data from one perforation. (a) The z component of the calculated tip position and our reference. The advantage of the use of the Kalman filter is evident in this case, since, as shown in (b), often no markers are detected.

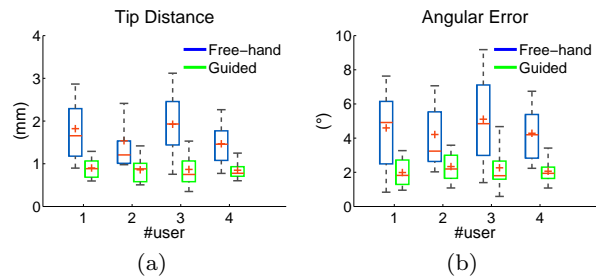


Fig. 18 Final accuracy in the screw placement on PB obtained by the users (EE group) when transferring the screw plan freehand (blue) and under guidance support (green): errors in (a) the tip distance d_T , and (b) total angle ψ .

We further investigated the performance of our algorithm by separately analyzing the feedback accuracy during targeting and during drilling. The two steps can be nicely separated using the z-coordinate of the drill bit delivered by our Polaris-based reference, which assumes positive values when the depth of the drill bit increases (the z-axis is positive towards the interior of the bone). Thus, when $z < 5$ we treat the corresponding action as targeting. When $z \geq 5$, we consider it an indication of drilling (see Table 3).

Table 3 Accuracy of the position feedback of the drill bit during targeting and during drilling. Mean and median values for the errors in the tip distance (d_{TG}), and for errors in the total angle (ψ_G) for: 1) All plastic bones (PB) for all users (AU), 16 right bones (64 screws) and 21 left bones (83 screws); 2) All forearm specimens (FS) (20 screws); 3) Only healthy forearm specimens (FSH) (12 screws); 4) Only forearm specimens with fractures (8 screws).

	Targeting				Drilling			
	d_{TG} (mm)		ψ_G ($^\circ$)		d_{TG} (mm)		ψ_G ($^\circ$)	
PB (AU)	1.95 ± 1.24	1.73	1.96 ± 1.22	1.88	2.15 ± 2.16	1.79	1.87 ± 1.74	1.73
FS	2.55 ± 1.59	2.36	2.67 ± 1.07	2.83	3.40 ± 3.55	2.47	2.74 ± 2.82	2.78
FSH	2.44 ± 1.74	2.24	2.30 ± 1.37	2.16	3.04 ± 3.92	2.47	2.48 ± 4.38	2.15
FSF	2.61 ± 1.49	2.44	2.89 ± 0.75	3.04	3.63 ± 3.28	2.47	2.91 ± 0.94	2.96

6 Discussion

We presented the integration of our portable guidance solution into our Unified-Planning-and-Guidance framework for distal radius fracture surgery. Our framework does not require the fixation of any navigation markers onto the patient: the patient reference is provided directly by registering the implant plate onto the X-ray images acquired intra-operatively. For guidance, minimal additional instrumentation is required, i.e. a set of small markers attached to the surgical drill sleeve and a video camera mounted onto the surgical drill.

The feasibility of our framework and its impact on the accuracy of screw positioning were investigated. For performance comparison, we recall the closest related work [32], a clinical study conducted using solely intra-operative planning. Though their results refer to real cases, we can still use them as a reference point for the expected accuracy without a guidance system: their reported errors in d_T , α and β are 2.24 ± 0.97 mm, $18.69 \pm 29.84^\circ$ and $1.66 \pm 4.46^\circ$ respectively [32].

The series of our evaluations conducted in a lab environment on phantoms (see Table 1), overall showed a significant increase in screw placement accuracy and robustness. The mean error in d_T and α was reduced by 55% and 80% respectively, while the standard deviation dropped by 42% and 85% accordingly. The mean error in β increased from 1.66° to 1.70° , while the standard deviation was more than halved. As expected, the error distribution (see Fig. 16) shows that higher errors occur when drilling in the north sector, i.e. close to the marker holder, since this reduces marker visibility. In these specific cases, appropriate drill sleeve rotation is expected to increase accuracy.

A similar performance was observed in the experiments conducted on the 5 forearm specimens, FS. Overall, the mean error in d_T and α was reduced by 32% and 75% respectively, while the standard deviation was decreased by 23% and 86% accordingly. The mean error in β increased from 1.66° to 2.92° , while the standard deviation was decreased by 41%.

In one of the right FSHs, the drill sleeve for one screw was rotated 90° w.r.t. the default position. Although our software allows selecting the preferred $\mathbf{T}_{H_1}^D$ for planning transfer, in this case it was not conveyed by the user. Even under such circumstances, our UPG framework helped keep the mean errors for both α and β below 10° and 4° respectively. With this case of incorrectly rotated drill sleeve, our evaluation for FSH results in errors in d_T , α and β of 1.94 ± 1.37 mm, $9.00 \pm 11.89^\circ$ and $3.32 \pm 2.98^\circ$ respectively [18].

Our sequential analysis over all the forearm specimens, FS, showed that the performance of the medical expert improved over time (see Fig. 13). The same behavior was observed on the bone phantoms. No training phase was performed before the experiments. It appears that user 5 needed some additional time to map how his movements influence the performance of the guidance system. On PBs across the series of experiments his accuracy in d_T , α and β increased respectively from: 1.80 ± 1.10 mm, $8.69 \pm 8.50^\circ$, $1.59 \pm 1.36^\circ$, to: 0.75 ± 0.24 mm, $2.86 \pm 1.01^\circ$, $1.06 \pm 0.81^\circ$. On FSs across the tests, his performance in d_T , α and β increased from 2.05 ± 1.59 mm, $6.49 \pm 6.96^\circ$, $4.33 \pm 5.48^\circ$, to: 1.58 ± 0.54 mm, $3.40 \pm 1.81^\circ$, $2.66 \pm 1.93^\circ$. According to our experimental design, the medical expert operated first on FSHs and at last on FSFs.

We analyzed the difference in the final accuracy in the screw placement obtained when a user transfers the same set of screw plans on PB, once freehand, and once guided by our UPG framework (see Fig. 18). As expected, both the mean error in d_T and ψ was reduced by 49% and 55% respectively when using our guidance system. The corresponding standard deviation dropped by 55% and 53%. Please note that the evaluation of freehand vs. guided was performed by users with engineering expertise, and it is not necessarily representative of how a medical doctor would perform. Unfortunately, there is no data about the accuracy of the screw placement for guided vs. freehand for medical experts. Thus, engineering experts were our best option.

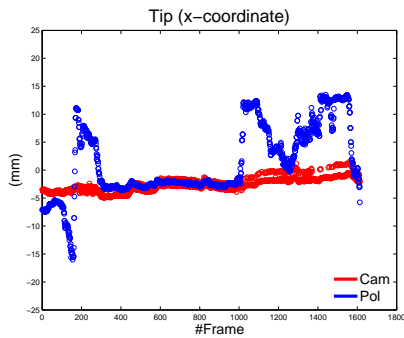


Fig. 19 Example of the position feedback for the drill bit tip obtained during one drilling operation on a fractured specimen by our drill-camera system (red) and by the Polaris system (blue). The high drift of the Polaris system is attributed to the relative movement between S_{DP} and S_D and does not reflect a real motion of the instrument. This relative movement is correctly not detected by our camera-drill system.

When analyzing the real-time position feedback of the drill bit (see Table 2), we observed that for the PB, as expected, the error in d_{TG} decreases with increased marker visibility. As the number of visible markers increases, the pose recovery algorithm [15] exploits the non-planar distribution of our markers, and consequently of the feature points, which are used for pose reconstruction. The orientation is also nicely estimated even when only one marker is visible. On FS, the median values in d_{TG} and ψ_G remain under 2.5 mm and 2.9° respectively. However, the expected correlation between a larger number of detected markers and higher accuracy does not hold anymore. The Kalman filter is employed when no markers are visible or there is a high angle difference between consecutive frames. The errors in d_{TG} and ψ_G are 3.08 ± 3.83 mm and $3.46 \pm 5.70^\circ$ respectively. The maximum error was 46.11 mm and 55.36° in d_{TG} and ψ_G respectively, while the median was 2.06 mm and 1.45° respectively. The comparatively low median values indicate that there is a small number of relatively large outliers.

On PB and FS, during drilling, we observe a slight increase in the error in d_{TG} (see Table 3), which can be ascribed to the increase of image blur. There is also an increase in the standard deviation during drilling, particularly in the results of the forearm specimens. On FS the errors in d_{TG} and ψ_G tend to increase as the number of visible markers increases. This can be attributed to the relative movement of DP (the Polaris reference onto the drill sleeve) w.r.t. to the drill sleeve. When operating on the forearms, especially on the fractured ones, the surgeon needs to compress the joint at the distal radius during drilling to perform the reduction. The manner in which the forearm needs to be held at this point of the procedure increases the contact of the

forearm with DP, thus inducing a relative movement between DP and the drill sleeve. This introduces a temporary unreliability of our Polaris-based reference. This was observed when we analyzed the position of DP in the Polaris CS, S_P . An example is shown in Fig. 19: the relative movement between S_{DP} and S_D , which causes the high drift in the x value of the tip position estimated by the Polaris-based system, does not reflect a real movement of the instrument. This movement is correctly not detected by our camera-drill system.

Our guidance module requires a calibration step, which needs to be performed once when the camera is rigidly mounted onto the drill for the first time. It can be performed at any time before the surgery. The calibration needs to be repeated only in case of rearrangement of the camera mount onto the drill. Rearrangement can be avoided e.g. by integrating the camera mount directly into the design of the drill casing. Since it is a one-time procedure, it does not affect the operation time.

Our UPG framework was evaluated on PBs and on FSs. Further work needs to be performed to allow the translation of our framework onto patients. Additional miniaturization of the camera and its mount is expected to improve the maneuverability of the drill. This would also help reduce the impact of the camera-drill weight on the amount of axis bending, which could occur while drilling. Moreover, our UPG framework should be used only after stable cortical fixation of the implant plate, thus ensuring that no relative displacement between the bone of the patient and the implant plate occurs. If during the procedure re-positioning of the plate is required, the planning step needs to be repeated.

7 Conclusions

We have developed and evaluated a prototype framework for supporting orthopedic surgeons during an ORIF procedure. The support to the physician is provided from the beginning to the end of the procedure. Our evaluation shows that our UPG framework is expected to increase the accuracy in screw positioning and to improve robustness.

Acknowledgements This work was supported by the Research Training Group 1773 “Heterogeneous Image Systems”, funded by the German Research Foundation (DFG).

Conflict of interest J. Magaraggia, J. Hornegger, E. Angelopoulou, S. Vetter, and J. Franke have no conflict of interest. W. Wei, M. Weiten, G. Kleinszig and K. Barth are employees of Siemens Healthcare GmbH. At the time this work was performed, A. John and A. Egli

were funded by Siemens AG. The studies were carried out with the support from Siemens Healthcare GmbH, Erlangen, Germany.

References

- Al-Rashid, M., Theivendran, K., Craigen, M.: Delayed ruptures of the extensor tendon secondary to the use of volar locking compression plates for distal radial fractures. *Journal of Bone&Joint Surgery, British Volume* **88**(12), 1610–1612 (2006)
- Arora, R., Lutz, M., Hennerbichler, A., Krappinger, D., Espen, D., Gabl, M.: Complications following internal fixation of unstable distal radius fracture with a palmar locking-plate. *Journal of Orthopaedic Trauma* **21**(5), 316–322 (2007)
- Bose, R.: *Information theory, coding and cryptography*. Tata McGraw-Hill Education (2008)
- Bose, R.C., Ray-Chaudhuri, D.K.: On a class of error correcting binary group codes. *Information and control* **3**(1), 68–79 (1960)
- Cho, J., Sung, W.: Efficient software-based encoding and decoding of bch codes. *Computers, IEEE Transactions on* **58**(7), 878–889 (2009)
- Diotte, B., Fallavollita, P., Wang, L., Weidert, S., Thaller, P.H., Euler, E., Navab, N.: Radiation-free drill guidance in interlocking of intramedullary nails. In: MICCAI, Part I, *LNCS*, vol. 7510, pp. 18–25 (2012)
- Egli, A., Kleinszig, G., John, A., Fernandez, A., Cardelino, J.: Pose estimation quality assessment for intra-operative image guidance systems. In: *SPIE Medical Imaging*, vol. 86711 (2013)
- Fiala, M.: Artag fiducial marker system applied to vision based spacecraft docking. In: *IROS, Workshop on Robot Vision for Space Applications*, pp. 35–40 (2005)
- Franke, J., Vetter, S., Mühlhäuser, I., Grützner, P., von Recum, J.: Virtual implant planning system: First clinical results. *Bone & Joint Journal Orthopaedic Proceedings Supplement* **95**(SUPP 28), 76–76 (2013)
- Giannoudis, P.V., Campbell, D., Meier, R.: Fractures of the distal radius. In: P.V. Giannoudis, H.C. Pape (eds.) *Practical Procedures in Orthopaedic Trauma Surgery*. Cambridge University Press (2006)
- Jenny, J.Y., Miehle, R.K., Giurea, A.: Learning curve in navigated total knee replacement. A multi-centre study comparing experienced and beginner centres. *The Knee* **15**(2), 80–84 (2008)
- Joseph, S.J., Harvey, J.N.: The dorsal horizon view: detecting screw protrusion at the distal radius. *The Journal of Hand Surgery* **36**(10), 1691–1693 (2011)
- Koutenaie, B.A., Guler, O., Wilson, E., Thoranaghatte, R.U., Oetgen, M., Navab, N., Cleary, K.: Improved screw placement for slipped capital femoral epiphysis (SCFE) using robotically-assisted drill guidance. In: MICCAI, Part I, *LNCS*, vol. 8673, pp. 488–495 (2014)
- Kreuder, F.: *2D-3D-Registrierung mit Parameterentkopplung für die Patientenlagerung in der Strahlentherapie*. Dissertation, vol. 7. KIT Scientific Publishing (2009)
- Lu, C., Hager, G., Mjolsness, E.: Fast and globally convergent pose estimation from video images. *Pattern Analysis and Machine Intelligence, IEEE Transactions on* **22**(6), 610–622 (2000)
- Magaraggia, J., Kleinszig, G., Graumann, R., Angelopoulou, E., Hornegger, J.: A video guided solution for screw insertion in orthopedic plate fixation. In: *SPIE Medical Imaging*, vol. 86710 (2013)
- Magaraggia, J., Kleinszig, G., Wei, W., Weiten, M., Graumann, R., Angelopoulou, E., Hornegger, J.: On the accuracy of a video-based drill-guidance solution for orthopedic and trauma surgery: preliminary results. In: *SPIE Medical Imaging*, vol. 903610 (2014)
- Magaraggia, J., Wei, W., Weiten, M., Kleinszig, G., Vetter, S., Franke, J., Barth, K., Angelopoulou, E., Hornegger, J.: A portable intra-operative framework applied to distal radius fracture surgery. In: *MICCAI, Part I, LNCS*, pp. 323–330 (2015)
- Malepati, H.: *Digital media processing: DSP algorithms using C*. Newnes (2010)
- Markley, F.L., Cheng, Y., Crassidis, J.L., Oshman, Y.: Averaging quaternions. *Journal of Guidance, Control, and Dynamics* **30**(4), 1193–1197 (2007)
- Marziliano, P., Dufaux, F., Winkler, S., Ebrahimi, T.: A no-reference perceptual blur metric. In: *International Conference on Image Processing*, vol. 3, pp. 57–60. IEEE (2002)
- McKay, S.D., MacDermid, J.C., Roth, J.H., Richards, R.S.: Assessment of complications of distal radius fractures and development of a complication checklist. *Journal of Hand Surgery* **26**(5), 916–922 (2001)
- Nielsen, M.A., Chuang, I.L.: *Quantum computation and quantum information*. Cambridge university press (2010)
- Olson, E.: Apriltag: A robust and flexible visual fiducial system. In: *IEEE International Conference on Robotics and Automation*, pp. 3400–3407. IEEE (2011)
- Pichler, W., Grechenig, W., Clement, H., Windisch, G., Tesch, N.: Perforation of the third extensor compartment by the drill bit during palmar plating of the distal radius. *Journal of Hand Surgery (European Volume)* **34**(3), 333–335 (2009)
- Rikli, D.A., Campbell, D.A.: Distal radius and wrist. In: T.P. Rüedi, R.E. Buckley, Renner, C.G. Moran (eds.) *AO principles of fracture management*. Davos, Switzerland: AO Publishing (2007)
- Schichor, C., Schöller, K., Tanner, P., Uhl, E., Goldbrunner, R., Tonn, J.C., Witte, J.: Magnetically guided neuronavigation of flexible instruments in shunt placement, transsphenoidal procedures, and craniotomies. *Operative Neurosurgery* **63**(1), ONS121–ONS128 (2008)
- Schweighofer, G., Pinz, A.: Robust pose estimation from a planar target. *Pattern Analysis and Machine Intelligence, IEEE Transactions on* **28**(12), 2024–2030 (2006)
- Simic, P.M., Placzek, J.D.: Distal radius fractures. In: J.P. Stannard, A.H. Schmidt, K.P. J. (eds.) *Surgical Treatment of Orthopaedic Trauma*. Thieme (2011)
- Sügün, T., Karabay, N., Gürbüz, Y., Özaksar, K., Toros, T., Kayalar, M.: Screw prominences related to palmar locking plating of distal radius. *Journal of Hand Surgery (European Volume)* **36**(4), 320–324 (2011)
- Trucco, E., Verri, A.: *Introductory techniques for 3-D computer vision*, vol. 201. Prentice Hall Englewood Cliffs (1998)
- Vetter, S., Mühlhäuser, I., von Recum, J., Grützner, P.A., Franke, J.: Validation of a virtual implant planning system (vips) in distal radius fractures. *Bone&Joint Journal Orthopaedic Proceedings Supplement* **96**, 50–50 (2014)
- Wagner, D., Schmalstieg, D.: Artoolkitplus for pose tracking on mobile devices. In: *CVWW, 12th Computer Vision Winter Workshop* (2007)
- Zhang, X.: *VLSI Architectures for Modern Error-Correcting Codes*. CRC Press (2015)
- Zhao, Y., Cachard, C., Liebgott, H.: Automatic needle detection and tracking in 3d ultrasound using an ROI-based RANSAC and Kalman method. *Ultrasonic Imaging* **35**(4), 283–306 (2013)